IAC–25–B4,8,8,x101410

Assessing Control Robustness of CubeSat Propulsion Systems for (99942) Apophis Proximity Operations

Carmine Buonagura[a*], Carmine Giordano[b], Angelo Cervone[c], Francesco Topputo[d]

[a] *PhD Student, Department of Aeropace Science and Technology (DAER), Politencico di Milano, Via La Masa 34, carmine.buonagura@polimi.it*
[b] *PostDoc Fellow, Department of Aerospace Science and Technology (DAER), Politencico di Milano,Via La Masa 34, carmine.giordano@polimi.it*
[c] *Associate Professor, Department of Space Science, TU Delft,Mekelweg 5, a.cervone@tudelft.nl*
[d] *Full Professor, Department of Aerospace Science and Technology (DAER), Politencico di Milano, Via La Masa 34, francesco.topputo@polimi.it*
[*] *Corresponding author*

Abstract

The exploration of minor celestial bodies is gaining increasing attention due to its scientific relevance, engineering challenges, and implications for planetary defense. Simultaneously, the use of miniaturized platforms such as CubeSats is expanding due to their lower development, qualification, and launch costs. Their cost-effectiveness enables higher-risk operations, making them well suited for proximity missions around minor bodies. The RAMSES mission embodies these two concepts, with the mothercraft RAMSES set to reach (99942) Apophis and conduct in-depth studies during its close encounter. The mission will deploy two 6U CubeSats, RCS-1 and RCS-2, to characterize the asteroid. The dynamical environment in proximity of asteroids is highly uncertain, with perturbations playing a significant role. Therefore, robust orbital and attitude guidance and control strategies are essential for ensuring mission success under varying conditions. To address this challenge, this study presents a 6-DoF guidance and control simulation framework for proximity operations along hyperbolic trajectories near minor bodies, with a specific focus on (99942) Apophis. An optimization algorithm is developed to integrate attitude dynamics with trajectory design while accounting for the performance and technological constraints of CubeSat propulsion systems. This approach evaluates the feasibility of employing miniaturized propulsion technologies in a minor body environment. The analysis explores 4 different propulsion technologies, namely bipropellant, monopropellant, cold gas, and resistojet, and 10 orbital distances to determine the feasibility of flying hyperbolic arcs. Based on the proposed methodology, the results indicate that a minimum thrust of 8 mN is required to enable such trajectories. Additionally, key performance metrics, including observation time, firing time, propellant consumption, and pointing accuracy, are analyzed. The values and trends of these parameters are presented as functions of thrust level and orbital distance.

1. Introduction

The exploration of minor bodies has gained significant momentum, driven by scientific interest, technological advancements, and potential resource utilization [1–3]. These objects present a broad spectrum of sizes, shapes, and mass distributions [4, 5], which give rise to a weak and strongly nonlinear gravitational dynamical environments, further influenced by unpredictable perturbations such as Solar Radiation Pressure (SRP). As a result, the orbital and attitude dynamics of spacecraft operating in their vicinity are particularly complex and require robust strategies to account for the large uncertainties, since many of the system parameters can only be coarsely inferred from ground-based observations [6]. In parallel, the advent of low-cost manufacturing and launch opportunities has spurred increasing interest in CubeSats for proximity operations around minor bodies, as their low cost makes them suitable for high-risk missions.

Although numerous interplanetary CubeSat concepts have been studied or proposed for future missions to minor bodies [7–9], to date, only six missions, and no CubeSats, have operated in close proximity to such bodies. These missions include NEAR [10], Hayabusa-I [11], Dawn [12], Rosetta [13], Hayabusa-II [14], and OSIRIS-REx [15]. The only exception is LICIACube [16], which, however, performed a flyby of asteroid (65803) Didymos.
Two missions have been confirmed to conduct scientific investigations near asteroids. In 2027, the 6U CubeSats Milani [17] and Juventas [18] will accompany the Hera [19] platform to the asteroid (65803) Didymos to study the consequences of the DART impact [20, 21]. Additionally, the RAMSES mission, scheduled for 2029, will deploy two 6U CubeSats [22], RCS-1 and RCS-2, near asteroid (99942) Apophis during its close encounter with Earth.

The mission aims to assess the effects of Earth's strong gravitational pull on the asteroid.
Various studies have explored guidance and control methods for close proximity operations around minor bodies. In [23], robust orbital guidance and control algorithms are developed to handle uncertainties during the approach and hovering phases of asteroids (101955) Bennu and (433) Eros, eliminating the need for extensive navigation campaigns. This work uses the cannonball model to account for SRP and targets circular trajectories, moreover the spacecraft attitude is not considered.
On the other hand, [24] simulates the approach and hovering of (101955) Bennu using autonomous navigation and orbit control. This study models the true SRP with a hypothetical spacecraft, assuming that its solar panels are always oriented toward the Sun. Maneuvers are represented as impulsive Δv, with the spacecraft attitude assumed to be ideal.
Additionally, [25] and [26] propose nonlinear landing and hovering control schemes designed for real-time onboard implementation, treating the spacecraft as a point mass. The orbital guidance and control strategy of Milani considering the cannonball model is deeply described in [27, 28]. Lastly, [29] introduces a high-fidelity 6-DOF simulator for asteroid landing scenarios, incorporating fixed propulsion system properties and utilizing reinforcement learning techniques.
Other studies that closely resemble spacecraft motion around minor bodies are those addressing the relative motion between multiple spacecraft in formation flying scenarios, due to the similarities in guidance and control strategies required in both contexts [30–32]. However, a comprehensive study that accurately couples trajectory design with attitude dynamics, specifically in the context of the RAMSES mission to characterize and optimize hyperbolic arcs around asteroid (99942) Apophis, is still missing. Given the importance of correction maneuvers and the associated attitude pointing accuracy for the RAMSES mission, having such a study would be highly valuable.
In this work, we solved a guidance and control optimization problem that accurately couples attitude dynamics and trajectory design for hyperbolic proximity arcs around (99942) Apophis, assessing the feasibility of such trajectories for different propulsion technologies. The most common propulsion systems for such trajectories have been considered, namely bipropellant, monopropellant, cold gas, and resistojet. Their limitations in completing HAs in the vicinity of (99942) Apophis have been assessed. The effects of different minor body properties and a high-fidelity gravity field are discussed in [33].

The paper is organized as follows. Section 2 provides a detailed description of the asteroid and the platform. In Section 3, the algorithms implemented are thoroughly described. The results of the optimization and for the different propulsion systems are presented in Section 4. Finally, conclusions are discussed in Section 5.

2. Background

In this section, the properties of (99942) Apophis and of the platform are described.

2.1 Apophis

Several asteroids have a nonzero probability of impacting Earth, including (99942) Apophis, an elongated, irregularly shaped asteroid that will make a close approach to Earth on April 13, 2029. This event presents a unique opportunity to study its properties, refine its orbital parameters, and assess potential risks for future encounters. In this work, (99942) Apophis, a Near-Earth Asteroid (NEA), with its physical properties reported in Table 1 and its orbital elements listed in Table 2.

$\boldsymbol{R_{SB}}$ [km]	0.221
$\boldsymbol{\mu}$ [km^3/s^2]	3.00×10^{-9}
RA [deg]	250
Dec [deg]	-75
Period [h]	27.38

Table 1. Relevant properties of (99942) Apophis.

a [AU]	e [$-$]	i [deg]	Ω [deg]	ω [deg]
1.47	0.56	6.35	35.5	286

Table 2. Minor body trajectory orbital elements.

The main assumption considered is that the minor body is at its minimum distance from the Sun, approximately 0.65 AU, and that the Earth is positioned along its orbit at the point of minimum distance from the minor body. This orbital configuration enables testing the feasibility of hyperbolic trajectories under the most challenging conditions, where SRP and the third-body perturbations from the Sun and Earth are particularly significant. The assumption that the Sun–minor body vector remains constant is justified due to the short mission duration considered in our analyses.

2.2 Platform

The platform considered in this work is a 6U CubeSat, identical to the one proposed for the Milani mission [28], representing the baseline for Ramses CubeSat 1 (RCS-1). Considering the CubeSat body-fixed frame, the scientific payload is assumed to point along the positive x-axis, while the main propulsion system is located on the same axis but on the opposite face of the spacecraft. The solar panels are aligned with the z-axis, with their normal oriented toward the positive y-axis. These panels are fixed in this configuration, as there is no mechanism to allow their rotation. It is also assumed that the spacecraft center of mass (CoM) is displaced from the platform geometric center by an amount modeled as zero-mean white Gaussian noise.

$$\begin{aligned} \Delta \mathbf{r}_{CoM} &= N(0, \Delta r^2_{CoM,max}/9) \\ \text{where} \quad \Delta r_{CoM,max} &= 1.5\,\text{cm} \end{aligned} \tag{1}$$

A CubeSat schematic representation, along with the body reference frame, and relevant normal vectors are reported in Figure 1.

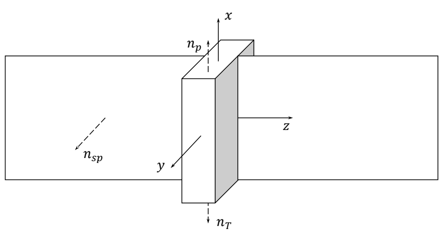

Fig. 1. Schematic representation of the 6U platform. n_p, n_{sp}, and n_T represent the normal vectors of the payload, solar panels, and thruster, respectively.

The CubeSat mass m_{SC} is 12 kg, including 1 kg of propellant mass m_{prop}. An equivalent reflectivity coefficient $C_r = 1.24$ is considered.

The CubeSat will fly hyperbolic trajectories in the vicinity of the asteroid. Specifically, the minimum distance of the trajectory key points from the body center of mass is set to $3R_{SB}$ where R_{SB} represents the equivalent radius of the body. The maximum distance is set to $1.2r_{SOI}$, where r_{SOI} is the radius of the Sphere of Influence (SOI) of the body.

$$r_{SOI} = r_{B-S}\left(\frac{m_A}{m_S}\right)^{2/5} \tag{2}$$

where r_{B-S} is the distance of the minor body from the Sun, and m_A and m_S (1.9891×10^{30} kg) are the masses of the body and the Sun, respectively. These limiting distances have been chosen for safety reasons to mitigate the risks of impact and escape from the body.

3. Methodology

3.1 Equations of motion

The dynamical models presented in this work encompass both orbital dynamics and attitude dynamics and kinematics, taking into account the effects of mass evolution due to spacecraft maneuvers.

Orbital dynamics The spacecraft orbital dynamics in the vicinity of low-gravity bodies such as asteroids and comets is highly nonlinear and influenced by perturbations such as SRP and third-body effects. Specifically, considering a J2000 inertial frame centered at the minor body center of mass, the acceleration experienced by the CubeSat can be divided into various contributions, expressed in this frame:

$$\ddot{\mathbf{r}} = \mathbf{a}_b + \mathbf{a}_{SRP} + \mathbf{a}_{3b,s} + \mathbf{a}_{3b,p} + \mathbf{a}_T \tag{3}$$

where $\mathbf{a}_b$ represents the acceleration due to the small body, computed using the point mass model, as it is assumed that the CubeSat remains outside the minor body Brillouin sphere

$$\mathbf{a}_b = -\frac{\mu}{r^3}\mathbf{r} \tag{4}$$

where μ is the gravitational parameter of the minor body, and $\mathbf{r}$ and r represent the position and distance of the spacecraft relative to the body center of mass, respectively.

The acceleration due to SRP is denoted as $\mathbf{a}_{SRP}$, calculated as the sum of the contributions from each CubeSat face illuminated by the Sun.

$$\mathbf{a}_{SRP} = \begin{cases} A_{BN}\mathbf{a}_{SRP,B} & \text{if } -\hat{\mathbf{r}}_{C-S,B}\cdot\mathbf{n}_i > 0 \\ \mathbf{0} & \text{if } -\hat{\mathbf{r}}_{C-S,B}\cdot\mathbf{n}_i \leq 0 \end{cases} \tag{5}$$

where n_i is the ith normal vector of the platform surface and $\mathbf{a}_{SRP,B}$ is the SRP in the body frame. The SRP is then computed in the inertial frame by rotating its value from the spacecraft body-fixed frame using the rotation matrix A_{BN}.

The third-body perturbations from the Sun and Earth are computed as

$$\mathbf{a}_{3b,pb} = (\mu_{pb} + \mu)\frac{\mathbf{r}_{b-pb}}{r^3_{b-pb}} - \mu_{pb}\frac{\mathbf{r}_{C-pb}}{r^3_{C-pb}} \tag{6}$$

where the subscript pb refers to the perturbing body, meaning the numerical values will differ depending on whether the Sun or Earth is considered. Specifically, μ_{pb} is the gravitational parameter of the perturbing body, while r_{b-pb} and r_{C-pb} are the position vectors of the minor body barycenter and the field point relative to the perturbing body, expressed in the minor body inertial frame.

Finally $\mathbf{a}_T$ represents the acceleration due to the spacecraft control actions, specifically provided by its main propulsion system. Its value can be computed as

$$\mathbf{a}_{T,B} = -A_{BN}T\frac{\mathbf{n}_T}{m_{SC}} \tag{7}$$

where T is the thrust generated by the spacecraft, and $\mathbf{n}_T$ is the normal vector of the face where the propulsion system is mounted. The resulting acceleration, computed in the body-fixed frame, is then rotated into the inertial frame using the A_{BN} rotation matrix. The attitude profile is expressed in terms of two angles: azimuth Az and elevation El. These angles are parametrized in time as third-order polynomial functions [34].

$$\begin{aligned} Az(t) &= a_1 + a_2 t + \frac{a_3}{2}t^2 + \frac{a_4}{6}t^3 \\ \text{where} \quad \mathbf{a}_m &= [a_1,\, a_2,\, a_3,\, a_4]^T \\ El(t) &= b_1 + b_2 t + \frac{b_3}{2}t^2 + \frac{b_4}{6}t^3 \\ \text{where} \quad \mathbf{b}_m &= [b_1,\, b_2,\, b_3,\, b_4]^T \end{aligned} \tag{8}$$

The firing direction vector $\mathbf{n}_T(t)$ is then computed as

$$\mathbf{n}_T(t) = [\cos Az(t) \cos El(t),\ \sin Az(t) \sin El(t), \sin El(t)]^T \tag{9}$$

$$\mathbf{n}_T(t) = \begin{bmatrix} \cos\big(Az(t)\big)\cos\big(El(t)\big) \\ \sin\big(Az(t)\big)\cos\big(El(t)\big) \\ \sin\big(El(t)\big) \end{bmatrix} \tag{10}$$

Attitude dynamics and kinematics The spacecraft attitude, represented as a quaternion, is propagated using the spacecraft kinematic equation

$$\dot{\mathbf{q}} = \frac{1}{2}\Omega(\boldsymbol{\omega})\mathbf{q} \tag{11}$$

Where ω is the spacecraft angular rate, and $\mathbf{q}$ is the spacecraft attitude quaternion, consisting of a vector part $\bar{v}$ and a scalar part s .

$$\mathbf{q} = \begin{bmatrix} s \\ \bar{\mathbf{v}} \end{bmatrix}; \quad s \in \mathbb{R}^1 \quad \bar{\mathbf{v}} \in \mathbb{R}^3; \tag{12}$$

The matrix $\Omega(\omega)$ is defined as:

$$\Omega(\boldsymbol{\omega}) = \begin{bmatrix} 0 & -\boldsymbol{\omega}^T \\ \boldsymbol{\omega} & -\boldsymbol{\omega}^\times \end{bmatrix} \tag{13}$$

where $[\cdot]^\times$ is the skew-symmetric or cross-product matrix. The kinematic equation is coupled with the dynamics equation to retrieve the spacecraft angular rate.

$$J\dot{\boldsymbol{\omega}} = J\boldsymbol{\omega} \times \boldsymbol{\omega} + \tau + \mathbf{u}_c \tag{14}$$

where J is the spacecraft inertia matrix, τ represents the external torques acting on the spacecraft, and $\mathbf{u}_c$ denotes the attitude control input. The external torque τ considered is induced by the SRP due to the displacement between the spacecraft center of mass and its geometric center. Specifically, it is computed as:

$$\tau = A_{BN} \sum_{i=1}^{10} \mathbf{f}_i \times \mathbf{a}_{SRP,B} m_{SC} \tag{15}$$

where $\mathbf{f}_i$ is the position of the center of the ith surface relative to the spacecraft CoM. While the attitude control consists of two terms, the gyroscopic effect feedforward compensation and the control authority $\mathbf{u}_a$

$$\mathbf{u}_c = \boldsymbol{\omega} \times J\boldsymbol{\omega} + \mathbf{u}_a \tag{16}$$

The control authority is implemented as a proportional–derivative (PD) control action, constrained by the maximum torque achievable by actuators on a 6U CubeSat*.

$$\mathbf{u}_a = -K_d \Delta\boldsymbol{\omega} - K_p \Delta\boldsymbol{\theta} \quad \text{with} \quad |\mathbf{u}_a| < 0.007 I\,\mathrm{N\,m} \tag{17}$$

where $\Delta\omega$ and $\Delta\theta$ are the angular velocity and attitude errors, calculated as the differences between the actual and desired values, and I is the 3×3 identity matrix. The gain matrices K_p and K_d are selected through a trial-and-error approach based on the phase of the mission, with different values considered for the firing, cruising, and slew phases, as detailed in Table 3. While optimizing the selected gains to account for the varying moments of inertia along the spacecraft principal axes could yield more refined results, the present study focuses on demonstrating the feasibility and effectiveness of the proposed control strategy using a non-optimized set of gains.

Mission phase	K_p [N m]	K_d [N m s]
Cruising	$3 \times 10^{-4} I$	$1 \times 10^{-2} I$
Firing	$30I$	$7 \times 10^{-2} I$
Slew	$3 \times 10^{-3} I$	$7.75 \times 10^{-2} I$

Table 3. Attitude control gains for the different simulation phases.

Mass dynamics The spacecraft mass shows an evolution only during the firing phase, when the thruster is active. During this phase, the mass can be propagated using the relation

$$\dot{m} = -\frac{T}{I_{sp} g_0} \tag{18}$$

where I_{sp} is the spacecraft specific impulse, and g_0 (9.81 m/s^2) is the standard gravitational acceleration at Earth's surface.

3.2 Statement of the problem

The final objective of this work is to assess the feasibility of hyperbolic trajectories close to minor bodies by minimizing the amount of propellant consumed along the trajectory. To achieve this, an optimization problem is

*CD-DEV.PD.CW-01, CubeWheel Gen 2 Product Description, Ver.1.01, `https://www.cubespace.co.za/uploads/7007f7f5-f682-49d6-94d3-13d2cf3c5a93.pdf`, Last accessed: December 20, 2024 formulated as a Nonlinear Programming (NLP) problem. The vector of optimization variables $\mathbf{y}$ is as follows

$$\mathbf{y} = [T_1,\, T_2,\, \Delta t_1,\, \Delta t_2^1,\, \Delta t_2^2,\, \mathbf{a}_m^1,\, \mathbf{b}_m^1,\, \mathbf{a}_m^2,\, \mathbf{b}_m^2,\, \mathbf{x}_k,\, m_f]^T \tag{19}$$

where T_1 and T_2 are the time instants of the second and third key points, respectively, Δt_1, Δt_2^1, and Δt_2^2 are the time durations of the first and second firings. It is important to note that the second maneuver is divided in two intervals, centered at T_1, to allow the optimizer to achieve an asymmetric firing before and after the second key point. As described in Eq. (8), $\mathbf{a}_m^1$, $\mathbf{b}_m^1$, $\mathbf{a}_m^2$, and $\mathbf{b}_m^2$ are the vectors of cubic polynomial coefficients describing the evolution of the azimuth Az and elevation El angles during both firings. The spacecraft states (position and velocity) at specific selected points along the trajectory are indicated as $\mathbf{x}_k$, and m_f is the final mass of the spacecraft.
The objective function $f(\mathbf{y})$, as mentioned above, is given by

$$f(\mathbf{y}) = -m_f \tag{20}$$

Minimizing the negative of the final mass m_f is equivalent to maximizing the final spacecraft mass, thereby minimizing propellant consumption.
This problem must be solved subject to a set of constraints. Firstly, initial conditions constraint can be defined, where the initial state and time are fixed to prescribed values: the starting time of the simulation and the first key point of the hyperbolic trajectory, respectively. The attitude is also constrained throughout the entire duration of the simulation to follow a desired attitude profile. These conditions can be summarized as

$$t_0 = t_0^{\cdot} \tag{21}$$

$$\mathbf{x}_0 = \mathbf{x}_0^{\cdot} \tag{22}$$

$$\mathbf{q}(t) = \mathbf{q}^{\cdot}(t) \tag{23}$$

The desired attitude $\mathbf{q}^{\cdot}$ is a function of the mission phase (firing, small-body pointing, slew), and will be discussed in Section 3.3.
A set of nonlinear inequality and equality constraints can also be defined. Specifically, with regard to the inequality constraints, it is imposed that the spacecraft must be inside a spatial cube when at the time instants of the second and third key points of the nominal hyperbolic trajectory, and the final eccentricity of the trajectory must be greater than 1.2. This eccentricity condition has been introduced as a safety margin to mitigate the risk of impact with the small body [27]. These conditions are expressed as

$$\mathbf{r}(T_1) \in C_1 \tag{24}$$

$$\mathbf{r}(T_2) \in C_2 \tag{25}$$

$$e(T_2) > 1.2 \tag{26}$$

where C_1 and C_2 represent two cubic regions, the extent of which depends on the distance of the key points from the minor body. Specifically, the size of their edges is equal to

$$l_C = 0.10 d_{SC-SB} \tag{27}$$

These regions have been assumed to be cubic to simplify the definition of constraints in the optimization. The nonlinear equality constraints depend on the multiple shooting algorithm [35] that has been implemented. Their goal is to minimize the position and velocity defects at each multiple shooting point and can be expressed as

$$\mathbf{x}(t) = \phi(\mathbf{x}_k, t_k, t_{k+1}) \quad \text{with} \quad k = 0, \ldots, m-1 \tag{28}$$

were m is the number of multiple shooting points. In this analysis, we consider $m = 4$. Specifically, these points are at the end of the first firing, before the slew maneuver from minor body pointing to firing, and before and after the second firing.
Lower bounds are set for the firing durations, corresponding to a value of 0.5 seconds.
Finally, the NLP problem can be formulated as follows

$$\min_{\mathbf{y}} f(\mathbf{y}) \quad \text{s.t.} \quad \begin{cases} t_0 = t_0^{\cdot} \\ \mathbf{x}_0 = \mathbf{x}_0^{\cdot} \\ \mathbf{q}(t) = \mathbf{q}^{\cdot}(t) \\ \mathbf{r}(T_1) \in C_1 \\ \mathbf{r}(T_2) \in C_2 \\ e(T_2) > 1.2 \\ \mathbf{x}(t) = \phi(\mathbf{x_k}, t_k, t_{k+1}) \\ \quad \text{with} \quad k = 0, \ldots, m-1 \end{cases} \tag{29}$$

$$\Delta t_1 \in [0.50,\, \infty] \tag{30}$$

$$\Delta t_2^1 \in [0.25,\, \infty] \tag{31}$$

$$\Delta t_2^2 \in [0.25,\, \infty] \tag{32}$$

A schematic trajectory with all the important parameters is shown in Figure 2.

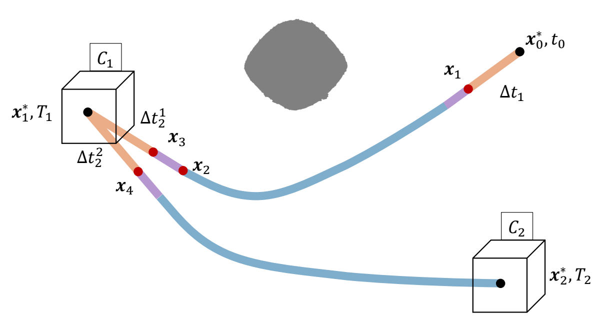

Fig. 2. Schematic representation of the hyperbolic trajectory considered along with some relevant parameters.

3.3 First guess generation

The first guess for the optimization problem is constructed following a three-step procedure.

Impulsive trajectory In the first step, considering only the point mass gravity of the small body and given two random points at a fixed distance from the body, a Lambert problem [36] is solved to determine the $\Delta v_{Lambert}$ required to transfer from one point to the other. Since there are multiple solutions depending on the time of flight, a zero-finding problem is solved to ensure that the trajectory eccentricity is equal to 1.2.

The second step involves incorporating all the perturbations present in the considered dynamical environment, as shown in Eq. (3). A simple shooting method is then applied to compute the initial spacecraft velocity, allowing the final propagated position to match the desired target point. Once the distance between the propagated position and the target one is below a certain tolerance, the problem is solved and the new impulsive maneuver Δv_{ss} is found.

Maneuver spreading At this point, as a third step, it is necessary to spread the impulsive maneuvers along the trajectory to properly simulate the propulsion system and the attitude evolution during firing. To do so, a constant attitude profile is considered for the generation of the first guess, and the firing time duration is computed based on the propulsion system properties.

$$\Delta t_{firing} = \frac{m_{SC}\Delta v_{ss}}{T} \tag{33}$$

Desired attitude computation The desired attitude varies across the three phases of the mission, and must be computed accordingly.

For the firing phase, the desired attitude depends on the thruster direction vector γ. Given that the thruster direction is along the x-axis in the spacecraft body frame, an eigen-axis, eigen-angle rotation can be used to compute the body-to-inertial frame rotation matrix required for the spacecraft attitude control. The desired angular velocity is set to the null vector.

For the small-body pointing phase, the desired rotation matrix is built to align the x-axis with the small body and minimize the angle between the solar panel normals and the Sun direction. This attitude will be referred to as power maximization (PM).

The desired quaternion representation can then be computed easily.

For the slew phase, an eigenaxis rotation slew maneuver is considered, which is a controlled rest-to-rest motion between two attitudes. The final desired attitude is either the firing mode or the minor body pointing mode, and the desired angular velocity is set to the null vector.

3.4 Propulsion systems selection

There is a wide spectrum of miniaturized propulsion systems tailored for CubeSats. Three broad categories can be distinguished: chemical, kinetic, and electrical [37]. In this analysis, electrical thrusters are not considered due to their limited thrust over power capabilities, which are not suitable for hyperbolic arcs. Chemical propulsion can be divided into bipropellant and monopropellant systems, while kinetic propulsion includes cold gas and resistojet systems. Regarding the resistojet, it is important to consider the amount of power available to the propulsion system. Consequently, the maximum thrust achievable with these systems, given an assumed available power of 100 W, can be determined. Specifically, for the resistojet, the maximum thrust achievable is 150 mN. The other propulsion systems considered are not significantly affected by the incoming power and for this reason a maximum thrust of 1 N is assumed to be a plausible value for miniaturized platforms like CubeSats. The properties of the propulsion systems considered in this work are reported in Table 4. To simplify the search space, the specific impulse has been fixed at the maximum value for the selected propulsion system.

Prop system	T_{rng} [mN]	T_{avg} [mN]	I_{sp} [s]
Biprop	$100 - 1000$	550	350
Monoprop	$20 - 1000$	510	250
Cold gas	$5 - 200$	102.5	80
Resistojet	$0.5 - 150$	75.25	150

Table 4. Selected propulsion systems properties.

3.5 Analyses performed

Two analyses were conducted to test the performance and robustness of propulsion systems in the proximity of minor bodies.

Variable thrust The key points of the hyperbolic trajectories were chosen to be at an average distance from the minor body, specifically

$$D_{kp} = \frac{D_{min} + D_{max}}{2} \tag{34}$$

The analysis was carried out considering the different propulsion systems, spanning the range of thrusts, to assess the feasibility of the trajectory and the minimum possible thrust required to fly these arcs.

Variable distance The thrust values for each propulsion system were fixed at the average value within the range of thrusts considered, and the distance from the minor body was allowed to vary from D_{min} to D_{max}. Specifically, ten different trajectories were considered for this analysis.

3.6 Performance metrics

It is required to define some metrics to assess the performance of the propulsion systems and control methods employed in our simulations. Four metrics have been defined, which will be further discussed below.

- **Observation time percentage**. It is the percentage of time along the trajectory when the spacecraft is pointing toward the minor body and scientific observations can be conducted. The condition that must be satisfied is
$$\hat{\gamma}(t) \cdot -\hat{r}(t) \geq 1 + \epsilon \tag{35}$$
where ϵ is a tolerance value depending on the desired pointing accuracy we want to achieve, 2 deg for our simulations.
The observation time can then be computed as
$$T_{obs} = \sum_{k=0}^{n} H[(\hat{\gamma}(t) \cdot -\hat{r}(t)) - (1 + \epsilon)](t_{k+1} - t_k) \tag{36}$$
where H is the Heaviside function. Consequently, the observation time percentage can be computed as
$$\eta_{obs} = \frac{T_{obs}}{T_2} \cdot 100 \tag{37}$$
- **Firing time**. This metric is the total firing time during the mission and can be computed as
$$\Delta t_{firing} = \Delta t_1 + \underbrace{\Delta t_2^1 + \Delta t_2^2}_{\Delta t_2} \tag{38}$$
- **Percentage of propellant consumed**. The consumed mass of propellant can be computed from the firing time Δt_{firing} as
$$m_{consumed} = \frac{T}{I_{sp} g_0} \Delta t_{firing} \tag{39}$$
Consequently, the percentage of propellant consumed is
$$m_p = \frac{m_{consumed}}{m_{prop}} \cdot 100 \tag{40}$$
- **Pointing accuracy**. This metric is used to assess the performance of the attitude control system. It is specifically evaluated during the minor body pointing phase, when precise pointing of the payload toward the minor body is required. The pointing accuracy δ_{point} is computed from the attitude error expressed in terms of quaternions.
$$\Delta \mathbf{q}(t) = \begin{bmatrix} \Delta \mathbf{q}_s(t) \\ \Delta \mathbf{q}_v(t) \end{bmatrix} = \mathbf{q}(t) \otimes \mathbf{q}_d(t) \tag{41}$$
where $\otimes$ represents the quaternion product, $\mathbf{q}$ is the true spacecraft attitude, and $\mathbf{q}_d$ is the desired quaternion at time t. The pointing accuracy is then determined as the norm of the vector part of the quaternion error.
$$\delta_{point} = \max ||\Delta \mathbf{q}_v|| \tag{42}$$

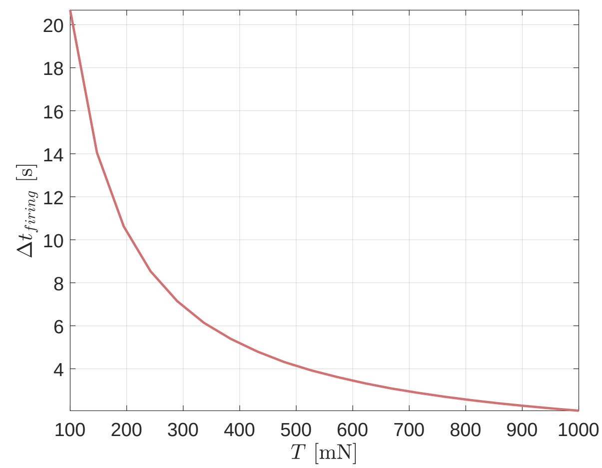

Fig. 3. Variable thrust Bipropellant.

4. Results

In this section, numerical results from the analyses of variable thrust and variable distance are provided.

4.1 Variable thrust

While the firing time exhibits a clear trend as thrust values increase, the other metrics remain largely consistent across the range of thrust values. For this reason, the firing time trends are graphically illustrated in Figures 3, 4, 5, and 6.

As expected, the firing time decreases monotonically with increasing thrust values. However, certain thrust values do not allow for feasible hyperbolic trajectories; these cases are indicated by a gray area in the figures. As depicted in the figures the minimum thrust value required for feasible trajectories is 8 mN for the specific case of (99942) Apophis.

4.2 Variable distance

The observation time percentage, firing time, propellant consumption, and pointing accuracy are reported for each propulsion system, with thrust held constant and

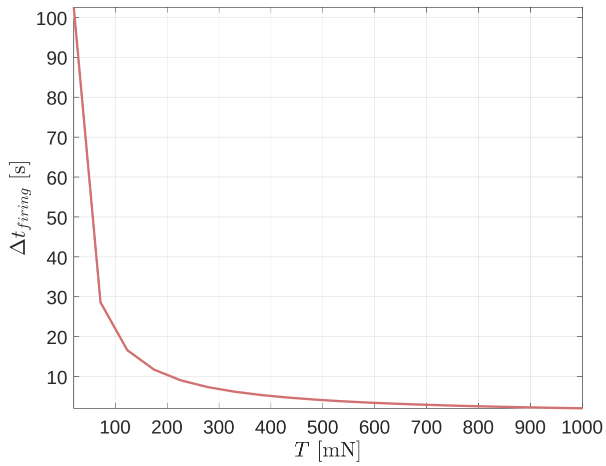

Fig. 4. Variable thrust monopropellant.

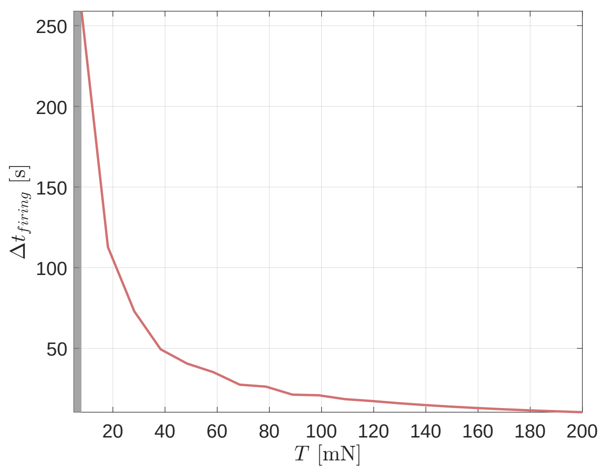

Fig. 5. Variable thrust cold gas.

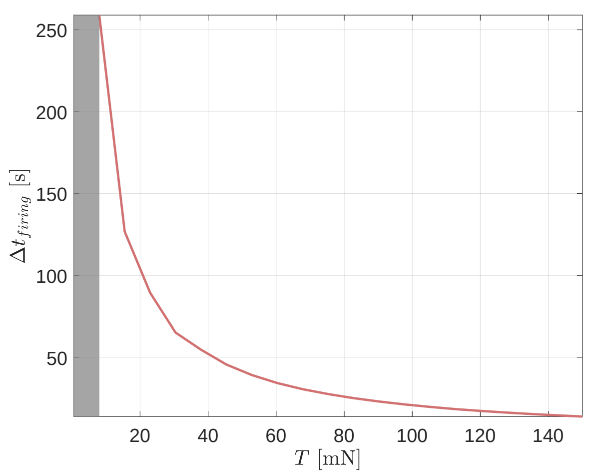

Fig. 6. Variable thrust resistojet.

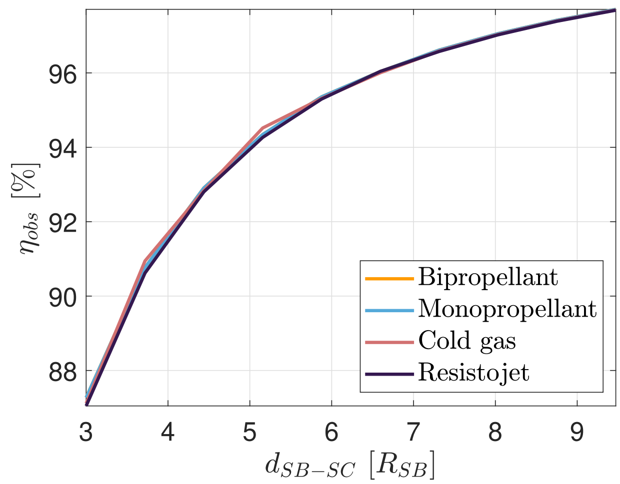

Fig. 7. Variable distance observation time percentage.

equal to the average value. The variable distance results are shown in Figures 7, 8, 9, and 10.

As the distance from (99942) Apophis increases, the observation time percentage increases consistently across all propulsion systems.

In contrast, the firing time decreases with increasing distance, with the effect being more significant for technologies with lower thrust. As a result, the resistojet exhibits the highest firing times at all distances, while the bipropellant and monopropellant systems overlap due to their similar thrust values.

The propellant consumption follows the same trend as the firing time and is primarily driven by the specific impulse: the lower the specific impulse, the higher the propellant consumption. Consequently, the cold gas thruster exhibits the highest propellant consumption, while the bipropellant system demonstrates the lowest.

Finally, the pointing accuracy decreases as the distance from the minor body increases. This is because the trajectory evolves more slowly at greater distances, enabling actuators to control and track the desired attitude profile more effectively.

5. Conclusion

An optimization problem was formulated and solved to assess the feasibility of executing hyperbolic arcs in the vicinity of asteroid (99942) Apophis under different propulsion system configurations. The results emphasize critical factors influencing the selection of propulsion technologies for such trajectories. Specifically, with a minimum feasible thrust requirement of approximately 8 mN, electric propulsion proves unsuitable for hyperbolic arcs in this context. Across all propulsion systems consid-

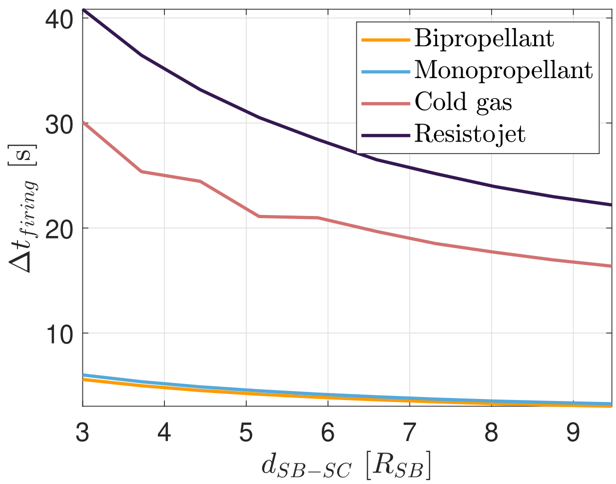

Fig. 8. Variable distance firing duration.

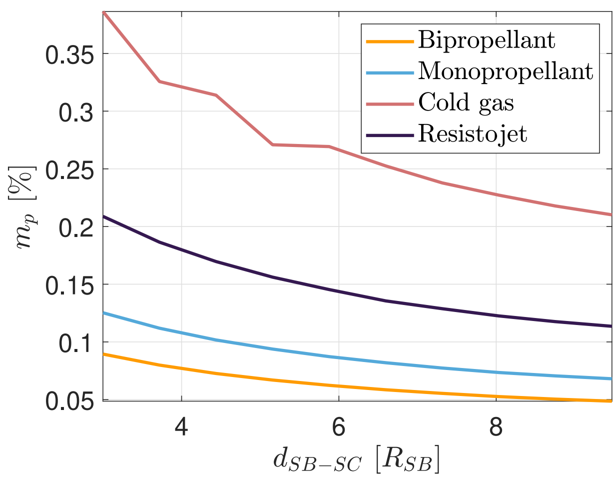

Fig. 9. Variable distance propellant consumption.

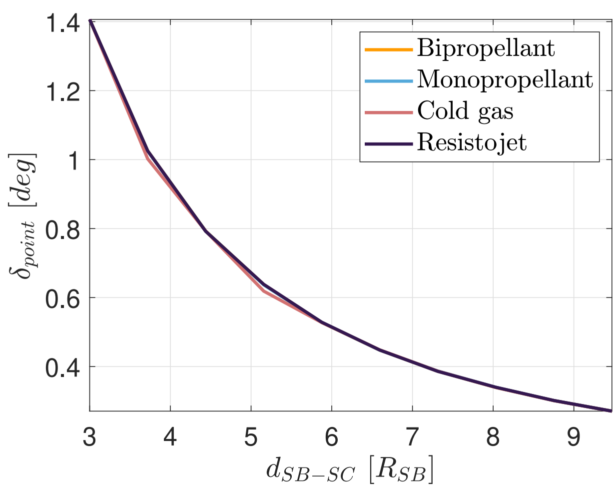

Fig. 10. Variable distance pointing accuracy.

ered, an increase in thrust consistently reduces firing duration, while observation time, propellant consumption, and pointing accuracy remain largely unaffected. Additionally, operating at greater distances from the minor body decreases firing duration, extends observation opportunities, lowers propellant consumption, and enhances pointing accuracy due to the slower evolution of the trajectory.

In conclusion, the findings provide mission designers with valuable guidelines for propulsion system selection and preliminary performance assessment for hyperbolic trajectories near asteroid (99942) Apophis, thereby supporting early-phase trade-off analyses and cost estimation.

Acknowledgment

This work was supported by the IDEA League Student Grants 2024.

This work was partially carried out as part of CASTOR, a project that has received funding from the European Union's Horizon Europe research and innovation programme under the Marie Skłodowska-Curie grant agreement no. 101103826.

6. References

[1] E. Asphaug, "Growth and evolution of asteroids," *Annual Review of Earth and Planetary Sciences*, vol. 37, pp. 413–448, 2009. doi: 10 . 1146 / ANNUREV.EARTH.36.031207.124214.

[2] M. Quadrelli et al., "Guidance, navigation, and control technology assessment for future planetary science missions," *Journal of Guidance, Control, and Dynamics*, vol. 38, no. 7, pp. 1165–1186, 2015. doi: 10.2514/1.G000525.

[3] K. Zacny, P. Chu, J. Craft, M. Cohen, W. James, and B. Hilscher, "Asteroid mining," in *AIAA SPACE 2013 Conference and Exposition*, 2013.

[4] W. F. Bottke Jr, A. Cellino, P. Paolicchi, and R. P. Binzel, "An overview of the asteroids: The asteroids iii perspective," *Asteroids III*, vol. 1, pp. 3–15, 2002.

[5] D. Morrison, "Asteroid sizes and albedos," *Icarus*, vol. 31, no. 2, pp. 185–220, 1977. doi: https:// doi.org/10.1016/0019-1035(77)90034-3.

[6] C. Buonagura, C. Giordano, F. Ferrari, and F. Topputo, "The orbital regime index: A comprehensive parameter to determine orbital regions around minor bodies," in *47th Rocky Mountain AAS GN&C Conference*, 2024.

[7] R. Walker et al., "Deep-space cubesats: Thinking inside the box," *Astronomy & Geophysics*, vol. 59, no. 5, pp. 5–24, 2018. doi: 10.1093/astrogeo/ aty237.

[8] F. Topputo et al., "Envelop of reachable asteroids by M-ARGO cubesat," *Advances in Space Research*, vol. 67, no. 12, pp. 4193–4221, 2021. DOI: 10.1016/j.asr.2021.02.031.

[9] A. S. French, Y. Takahashi, R. L. Anderson, S. Bhaskaran, S. Bandyopadhyay, and R. Amini, "Navigating a dual-spacecraft bistatic radar around an asteroid," in *33rd AAS/AIAA Space Flight Mechanics Meeting*, 2023.

[10] L. Prockter et al., "The NEAR Shoemaker mission to asteroid 433 eros," *Acta Astronautica*, vol. 51, no. 1, pp. 491–500, 2002, ISSN: 0094-5765. DOI: 10.1016/S0094-5765(02)00098-X.

[11] M. Yoshikawa, J. Kawaguchi, A. Fujiwara, and A. Tsuchiyama, "Hayabusa sample return mission," *Asteroids IV*, vol. 1, no. 1, 2015. DOI: 10.2458/azu_uapress_9780816532131-ch021.

[12] C. T. Russell and C. A. Raymond, "The dawn mission to vesta and ceres," in *The Dawn Mission to Minor Planets 4 Vesta and 1 Ceres*. New York, NY: Springer New York, 2012, pp. 3–23. DOI: 10.1007/978-1-4614-4903-4_2.

[13] K.-H. Glassmeier, H. Boehnhardt, D. Koschny, E. Kührt, and I. Richter, "The Rosetta mission: Flying towards the origin of the solar system," *Space Science Reviews*, vol. 128, pp. 1–21, 2007. DOI: 10.1007/s11214-006-9140-8.

[14] S.-i. Watanabe, Y. Tsuda, M. Yoshikawa, S. Tanaka, T. Saiki, and S. Nakazawa, "Hayabusa2 mission overview," *Space Science Reviews*, vol. 208, pp. 3–16, 2017. DOI: 10.1007/s11214-017-0377-1.

[15] D. S. Lauretta et al., "OSIRIS-REx: Sample return from asteroid (101955) Bennu," *Space Science Reviews*, vol. 212, pp. 925–984, 2017. DOI: 10.1007/s11214-017-0405-1.

[16] E. Dotto et al., "LICIACube - the light italian cubesat for imaging of asteroids in support of the NASA DART mission towards asteroid (65803) Didymos," *Planetary and Space Science*, vol. 199, p. 105 185, 2021. DOI: https://doi.org/10.1016/j.pss.2021.105185.

[17] M. Pugliatti et al., "The Milani Mission: Overview and Architecture of the Optical-Based GNC System," in *AIAA SCITECH 2022 Forum*, 2022.

[18] H. Goldberg et al., "The Juventas CubeSat in Support of ESA's Hera Mission to the Asteroid Didymos," in *33rd Annual AIAA/USU Conference on Small Satellites*, 2019.

[19] P. Michel et al., "European Component of the AIDA Mission to a Binary Asteroid: Characterization and Interpretation of the Impact of the DART Mission," *Advances in Space Research*, vol. 62, no. 8, pp. 2261–2272, 2018. DOI: 10.1016/j.asr.2017.12.020.

[20] S. Naidu et al., "Radar observations and a physical model of binary near-Earth asteroid 65803 Didymos, target of the dart mission," *Icarus*, vol. 348, p. 113 777, 2020, ISSN: 0019-1035. DOI: 10.1016/j.icarus.2020.113777.

[21] R. T. Daly et al., "An updated shape model of dimorphos from dart data," *The Planetary Science Journal*, vol. 5, no. 1, p. 24, 2024. DOI: 10.3847/PSJ/ad0b07.

[22] M. Kueppers, P. Martino, I. Carnelli, and P. Michel, "Ramses–esa's study for a small mission to apophis," in *AAS/Division for Planetary Sciences Meeting Abstracts*, vol. 55, 2023, pp. 201–08.

[23] R. B. Negri, A. F. B. A. Prado, R. A. J. Chagas, and R. V. Moraes, "Autonomous rapid exploration in close-proximity of asteroids," *Journal of Guidance, Control, and Dynamics*, vol. 47, no. 5, pp. 914–933, 2024. DOI: 10.2514/1.G007186.

[24] S. Takahashi and D. J. Scheeres, "Autonomous exploration of a small near-earth asteroid," *Journal of Guidance, Control, and Dynamics*, vol. 44, no. 4, pp. 701–718, 2021. DOI: 10.2514/1.G005733.

[25] R. Furfaro, D. Cersosimo, and D. R. Wibben, "Asteroid precision landing via multiple sliding surfaces guidance techniques," *Journal of Guidance, Control, and Dynamics*, vol. 36, no. 4, pp. 1075–1092, 2013. DOI: 10.2514/1.58246.

[26] R. Furfaro, "Hovering in asteroid dynamical environments using higher-order sliding control," *Journal of Guidance, Control, and Dynamics*, vol. 38, no. 2, pp. 263–279, 2015. DOI: 10.2514/1.G000631.

[27] F. Ferrari, V. Franzese, M. Pugliatti, C. Giordano, and F. Topputo, "Trajectory options for Hera's Milani cubesat around (65803) Didymos," *The Journal of the Astronautical Sciences*, vol. 68, no. 4, pp. 973–994, 2021. DOI: 10.1007/s40295-021-00282-z.

[28] C. Bottiglieri, F. Piccolo, C. Giordano, F. Ferrari, and F. Topputo, "Applied trajectory design for cubesat close-proximity operations around asteroids: The milani case," *Aerospace*, vol. 10, no. 5, 2023. DOI: 10.3390/aerospace10050464.

[29] B. Gaudet, R. Linares, and R. Furfaro, "Terminal adaptive guidance via reinforcement meta-learning: Applications to autonomous asteroid close-proximity operations," *Acta Astronautica*, vol. 171, pp. 1–13, 2020, ISSN: 0094-5765. DOI: 10.1016/j.actaastro.2020.02.036.

[30] D. Dumitriu, P. U. Lima, and B. Udrea, "Optimal trajectory planning of formation flying spacecraft," 1, vol. 38, 2005, pp. 313–318.

[31] Y. Chihabi and S. Ulrich, "Software-in-the-loop validation of a novel two-point optimal guidance for perturbed spacecraft rendezvous and formations," *The Journal of the Astronautical Sciences*, vol. 70, no. 5, pp. 1–45, 2023. DOI: https://doi.org/10.1007/s40295-023-00405-8.

[32] J.-F. Hamel and J. de Lafontaine, "Neighboring optimum feedback control law for earth-orbiting formation-flying spacecraft," *Journal of Guidance, Control, and Dynamics*, vol. 32, no. 1, pp. 290–299, 2009. DOI: https://doi.org/10.2514/1.32778.

[33] C. Buonagura, C. Giordano, A. Cervone, and F. Topputo, "Assessing control robustness of cubesat propulsion systems for minor body proximity operations," *Acta Astronautica*, vol. 237, pp. 174–187, 2025. DOI: https://doi.org/10.1016/j.actaastro.2025.07.068.

[34] D. A. Dei Tos, M. Rasotto, F. Renk, and F. Topputo, "LISA Pathfinder mission extension: A feasibility analysis," *Advances in Space Research*, vol. 63, no. 12, pp. 3863–3883, 2019. DOI: 10.1016/j.asr.2019.02.035.

[35] D. A. Dei Tos and F. Topputo, "High-fidelity trajectory optimization with application to saddle-point transfers," *Journal of Guidance, Control, and Dynamics*, vol. 42, no. 6, pp. 1343–1352, 2019. DOI: https://doi.org/10.2514/1.G003838.

[36] R. H. Battin, "Solving lambert's problem," in *An Introduction to the Mathematics and Methods of Astrodynamics, Revised Edition*. AIAA, 1999, ch. Chapter 7, pp. 295–364. DOI: 10.2514/5.9781600861543.0295.0364.

[37] S. Alnaqbi, D. Darfilal, and S. S. M. Swei, "Propulsion technologies for cubesats: Review," *Aerospace*, vol. 11, no. 7, 2024. DOI: 10.3390/aerospace11070502.